

Seismic imaging of mantle transition zone discontinuities beneath the northern Red Sea and adjacent areas

A. A. Mohamed,^{1,2} S. S. Gao,¹ A. A. Elsheikh,¹ K. H. Liu,¹ Y. Yu¹
and R. E. Fat-Helbary²

¹*Geology and Geophysics Program, Missouri University of Science and Technology, Rolla, MO 65409, USA. E-mail: sgao@mst.edu*

²*National Research Institute of Astronomy and Geophysics, Aswan Earthquake Research Center, Aswan, Egypt*

Accepted 2014 July 21. Received 2014 July 17; in original form 2014 January 30

SUMMARY

The dramatic asymmetry in terms of surface elevation, Cenozoic volcanisms and earthquake activity across the Red Sea is an enigmatic issue in global tectonics, partially due to the unavailability of broad-band seismic data on the African Plate adjacent to the Red Sea. Here, we report the first comprehensive image of the mantle transition zone (MTZ) discontinuities using data from the Egyptian National Seismic Network, and compare the resulting depths of the 410 and 660-km discontinuities with those observed on the Arabian side. Our results show that when a standard earth model is used for time-to-depth conversion, the resulting depth of the discontinuities increases systematically towards the axis of the Afro-Arabian Dome (AAD) from both the west and east. Relative to the westernmost area, the maximum depression of the 410-km discontinuity is about 30 km, and that of the 660-km discontinuity is about 45 km. The observed systematic variations can best be explained by a model involving a hydrated MTZ and an upper-mantle low-velocity zone beneath the AAD. Models invoking one or more mantle plumes originated from the MTZ or the lower-mantle beneath the study area are not consistent with the observations.

Key words: Computational seismology; Continental tectonics: extensional; Hotspots.

1 INTRODUCTION

The Red Sea is the archetype of nascent oceanic basins, which are the direct consequences of continental rifting. Rifting of the Africa-Arabian Plate along the Red Sea initiated at about 30 Ma, contemporaneous with the Trap Series basalts in the Afar area (Civetta *et al.* 1978; Camp & Roobol 1992; Stern & Johnson 2010; Lazar *et al.* 2012). Uplift of the Afro-Arabian Dome (AAD, Fig. 1) and the associated volcanism started at about 14 Ma and continues until the present time (Almond 1986; Camp & Roobol 1992; Bosworth *et al.* 2005; Pallister *et al.* 2010). The axis of the Red Sea and that of the AAD form an angle of about 25° from each other (Fig. 1). Both the early (30–14 Ma) and latter (14–0 Ma) phases of volcanism and the uplift of the AAD since 14 Ma are concentrated on the Arabian Plate and not the African Plate, leading to a dramatic asymmetry in topography, volcanism and current tectonic activity across the Red Sea.

While the majority of recent studies have attributed the pre-14 Ma rifting of the Red Sea to passive lithospheric extension probably originating from slab-pull of the subducted Arabian Plate beneath Eurasia, the mechanism leading to the uplift and volcanism of the AAD remains controversial (see recent reviews by Stern & Johnson 2010 and Lazar *et al.* 2012). Camp & Roobol (1992) proposed that the uplift and volcanism were associated with the upwelling flow of

a mantle plume beneath the central AAD, while Chang & van der Lee (2011) suggested the existence of a mantle plume beneath the northern AAD with a cylindrical low-velocity zone (LVZ) extending to the lower mantle from the surface. Dixon *et al.* (1989) argued that the Red Sea asymmetry is due to the northward migration of the Afar mantle plume to Saudi Arabia before 30 Ma.

In the study area, virtually all of the recent seismic tomography studies (Seber & Mitchell 1992; Ritsema *et al.* 1999; Rodgers *et al.* 1999; Debayle *et al.* 2001; Grand 2002; Benoit *et al.* 2003; Park *et al.* 2007, 2008; Sicilia *et al.* 2008; Chang *et al.* 2010; Chang & van der Lee 2011; Hansen *et al.* 2012) have suggested that a LVZ with a 1–2 per cent P -wave velocity (V_p) reduction and up to 5 per cent V_s reduction in the mantle beneath the AAD are responsible for the uplift of the AAD, probably through thermostatic buoyancy. Most of the studies limit the LVZ beneath the study area to the upper mantle, but in a few of them the LVZ extends to or below the mantle transition zone (MTZ) with a reduced velocity anomaly (Grand 2002; Chang *et al.* 2010; Chang & van der Lee 2011; Hansen *et al.* 2012). Based on seismic tomography and shear wave splitting measurements (Wolfe *et al.* 1999; Hansen *et al.* 2006), Chang *et al.* (2011) suggested that the uplift was the consequence of upper-mantle horizontal flow, probably originated from the Afar plume which tilts towards the northeast with increasing depth and thus is not being fed by the southern African superplume. In the

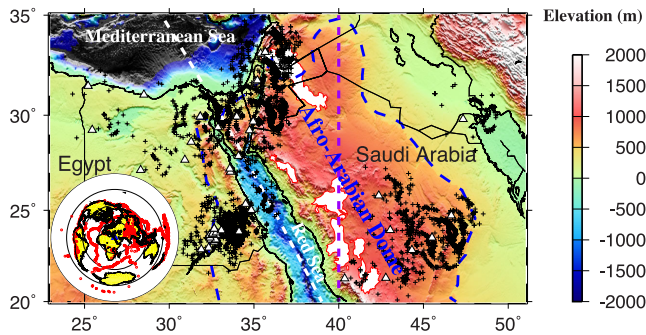


Figure 1. A topographic relief map of the study area showing the seismic stations (triangles) used in the study, the ray-piercing points (pluses) at 535-km depth, and the Cenozoic volcanic rocks (white areas). The dashed white line is a great-circle arc approximately along the Red Sea axis, the dashed purple line is the axis of the northern part of the Afro-Arabian Dome, which is outlined by the dashed blue curves and the inset shows the distribution of earthquakes used in the study. The concentric circles in the inset mark a 45° increment of epicentral distances.

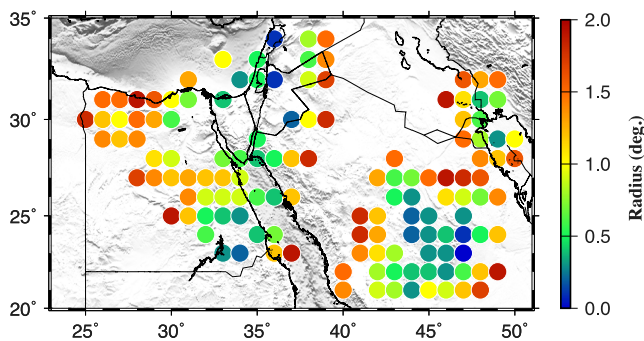


Figure 2. Spatial distribution of the circles containing 20 RFs. The colour represents the radius of the circles (in degrees).

study area (Fig. 1), a lower-mantle plume beneath northern Arabia approximately centred at 36°E and 32°N is proposed, and an N–S oriented zone of low shear wave velocity (V_s) with an upper-mantle average of about 5 per cent is revealed beneath western Saudi Arabia (Fig. 2 in Chang & van der Lee, 2011). This zone is spatially consistent with the zone of thinned lithosphere revealed by S -to- P receiver functions (RFs, Hansen *et al.* 2007).

Seismological and mantle xenolith investigations have suggested that the mantle portion of the lithosphere beneath the AAD is about 30–40 km thick, which is significantly thinner than most cratonic areas (McGuire & Bohannon 1989; Altherr *et al.* 1990; Hansen *et al.* 2007). In contrast, the crust beneath the same area has a normal or slightly greater-than-normal thickness of about 40 km (Mechie & Prodehl 1988; Sandvol *et al.* 1998; Kumar *et al.* 2002; Al-Damegh *et al.* 2005). The difference in the amount of thinning of these two layers suggests possible lower lithospheric erosion (Lazar *et al.* 2012), probably due to the northward flow from the Afar plume (Daradich *et al.* 2003). A recent shear wave splitting study by Elsheikh *et al.* (2014) using data from both Egypt and Arabia revealed uniform N–S fast orientations across the study area (Fig. 1). The observed N–S-oriented anisotropy was interpreted as the result of simple shear between the partially coupled lower lithosphere and upper asthenosphere associated with northward subduction of the African/Arabian plates.

The MTZ separates the upper and lower mantle. On a global scale, the top and bottom boundaries of the MTZ are approximately located at the depths of 410 and 660 km, respectively, and are thus

termed as the 410- and 660-km discontinuities (hereafter referred to as $d410$ and $d660$, respectively). Mineral physics and seismological investigations have suggested that the $d410$ represents the transition from olivine to wadsleyite, and the $d660$ represents the transition from ringwoodite to perovskite (Ringwood 1975). Under normal temperature and anhydrous conditions, the estimated Clapeyron slope of the transition across the $d410$ ranges from +1.5 to +3.0 MPa K^{−1}, and that across the $d660$ ranges from −4.0 to −2.0 MPa K^{−1} (Ringwood 1975; Bina & Helffrich 1994), implying that a higher-than-normal temperature would depress the $d410$ and uplift the $d660$ and vice versa. The presence of water in the MTZ has similar effects as reduced temperature (Litasov *et al.* 2005; Ohtani & Litasov 2006). Under high temperature conditions (e.g. ≥ 1700 °C), however, the phase transition across the $d660$ is dominated by the transition from majorite to perovskite, which has a positive Clapeyron slope of about +1.0 MPa K^{−1} (Hirose 2002). The depth of the MTZ discontinuities can thus be used to infer the *in situ* temperature in the MTZ and consequently provides constraints on the depth extent of possible mantle upwellings (Shearer 1991; Gao *et al.* 2002; Liu *et al.* 2003; Liu & Gao 2006; Andrews & Deuss 2008; Jasbinsek *et al.* 2010; Cao & Levander 2010; Gao & Liu 2014), which are presumably hot. Beneath Arabia, MTZ thickness can also provide constraints on the formation mechanisms for uplift of the AAD. Using broad-band seismic data from eight stations located in southern Saudi Arabia, Kumar *et al.* (2002) revealed significantly delayed (relative to global averages) P -to- S converted phases (P_{ds}) from the $d410$ and $d660$, and suggested that the delays are the results of low-velocity anomalies in the upper mantle (above the $d410$). They also found that the MTZ beneath the study area has a normal or slightly thicker-than-normal thickness. Similar conclusions were reached by Nyblade *et al.* (2000) and Benoit *et al.* (2003).

Due to the lack of coverage by broad-band seismic stations on the African Plate west of the northern Red Sea, previous MTZ and other seismological investigations in the area were mostly limited to the Arabian side. Such an asymmetry in data availability prevented in-depth investigations of the crustal and mantle structure, which is possibly related to the asymmetry in surface topography, volcanics and earthquake activity between the two plates on the opposing sides of the Red Sea. In this study, we use a combination of publicly accessible broad-band seismic data and data recorded by the Egyptian National Seismic Network (ENSN) to image MTZ discontinuities on both sides of the northern Red Sea, approximately beneath the area from 24° to 50°E and from 20° to 34°N (Fig. 1).

2 DATA AND METHODS

The three-component broad-band seismic data used in this study were obtained from two sources. Data from stations located east of the Red Sea were obtained from the Incorporated Research Institutions for Seismology (IRIS) Data Management Center (DMC) for the recording period between early 1990 and mid-2013. The rest of the data were recorded by the ENSN for the time period between late 2010 and the end of 2012. The cut-off event magnitude used for the requested data is calculated using $M_c = 5.2 + (\Delta - 30.0)/(180.0 - 30.0) - D/700.0$, where Δ is the epicentral distance, which ranges from 30° to 180°, and D is the focal depth in km (Liu & Gao 2010). The original broad-band data were bandpass filtered with a four-pole and two-pass Bessel filter in the frequency band of 0.02–0.5 Hz, and were converted into radial RFs using the procedure of Ammon (1991). Prior to the calculation of

the RFs, we mask the *PP* arrival using a set of exponential functions since *PP* has a very different ray-parameter than the direct *P* wave and thus can degenerate the resulting RFs (Gao & Liu 2013). A total of 6081 high-quality RFs from 49 stations are used in this study (Fig. 1). 34 of the stations belong to the ENSN and 15 are from the DMC. To our knowledge, this is the first time data from the ENSN stations have been used to image MTZ discontinuities.

For each of the RFs, we compute the geographic coordinates of the ray-piercing point at approximately the middle of the MTZ (535 km) using the IASP91 earth model and a non-plane wave assumption (Gao & Liu 2013). We then moveout-correct (based on IASP91) and stack the RFs with piercing points in consecutive circles. The distance between the centre of neighbouring circles is 1° . Each circle contains 20 piercing points, and thus the radii of the circles are a function of the spatial distribution of the piercing points. To ensure spatial coherence, results from a circle are not used if the radius is greater than 2° . Fig. 2 shows the location and size of the circles. We experimented with different combinations of the maximum allowable radius of the circles and the number of RFs in the circles, and we found that the above combination gave the optimal balance between spatial resolution and the detectability of the *d*410 and *d*660 arrivals in the stacking results.

To stack the RFs in a given circle, we place a candidate discontinuity at every kilometre in the top 800 km of the Earth. For each candidate discontinuity, the non-plane wave *P_ds* moveout time for each of the RFs is obtained based on the ray-parameters of the direct *P* wave and the converted *S* wave (Gao & Liu 2013). The RFs, which are time-series, are then converted into depth series by stacking the amplitude on each of the RFs corresponding to the *P_ds* moveout times, that is,

$$S(d) = \frac{1}{N} \sum_{i=1}^N S_i \left[T_i^{(d)} \right], \quad (1)$$

where $S(d)$ is the stacking amplitude for a candidate discontinuity at depth d , N is the number of RFs in the circle ($N = 20$ for this study), $T_i^{(d)}$ is the *P_ds* moveout time of the i th RF at depth d and $S_i(T_i^{(d)})$ is the amplitude of the i th RF at time $T_i^{(d)}$ (Gao & Liu 2013).

The stacking method assumes a uniform velocity structure in the area sampled by the *P* and *P_ds* ray paths beneath the circle, and consequently, lateral variations in the velocity structure lead to reduced stacking amplitude and a broadened peak with reduced amplitude corresponding to the discontinuity. The average MTZ discontinuity depths and their associated uncertainties are estimated using 20 bootstrap resampling iterations (Efron & Tibshirani 1986; Liu *et al.* 2003). Numerical tests show that given the number of RFs (20) included in the stacking for each circle, 20 iterations are appropriate to obtain reliable results.

Due to the use of a 1-D velocity model, the resulting MTZ depths are the true depths only under the special situation when there are no velocity anomalies above the discontinuities. The apparent (H_A) and true (H_T) thickness of a layer are related by (Gao & Liu 2013)

$$H_A = \frac{V_{p0} + \delta V_p - V_{s0} - \delta V_s}{(V_{s0} + \delta V_s) \times (V_{p0} + \delta V_p)} \times \frac{V_{p0} \times V_{s0}}{V_{p0} - V_{s0}} H_T, \quad (2)$$

where V_{p0} and V_{s0} are the mean *P*- and *S*-wave velocities in the standard earth model in the layer, and δV_p and δV_s are the *P*- and *S*-wave velocity anomalies in the layer. To calculate the apparent depth (D_A) of a discontinuity with a true depth of D_T for a given relative V_p anomaly, η , which is defined as $d \ln(V_p)$, and a $d \ln(V_s)$ of 2η , we first interpolate the IASP91 so that it has a uniform vertical interval of 1 km. For each 1-km thick layer (i.e. $H_T = 1$ km) from the surface

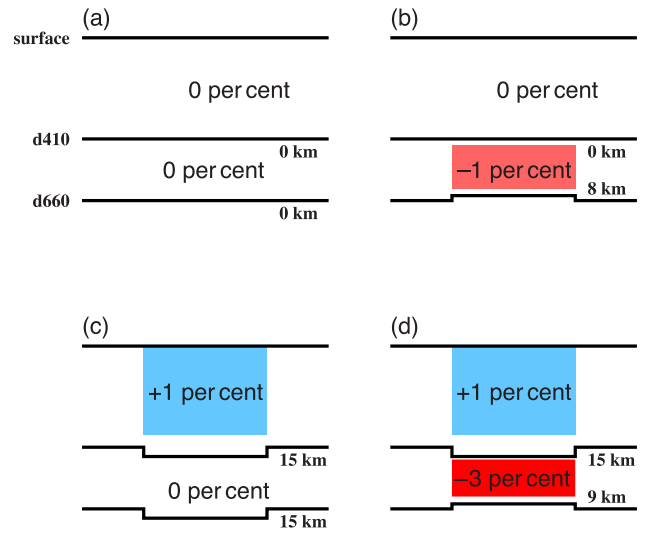


Figure 3. Schematic diagrams showing the effects of artificially introduced velocity anomalies on the observed MTZ discontinuity depths. (a) The real situation in which there are no velocity anomalies and undulations of MTZ discontinuities. (b) Artificial uplifting of *d*660 when an erroneous low-velocity anomaly is introduced in the MTZ and is used for depth corrections. (c) Artificial depression of both discontinuities when a high-velocity anomaly is introduced in the upper mantle. (d) Artificial *d*410 depression and *d*660 uplift when a high-velocity anomaly is introduced in the upper mantle and a low-velocity anomaly is introduced in the MTZ. Note that the amplitudes of the MTZ discontinuity undulations are vertically exaggerated by a factor of 2.5.

to D_T , the velocity anomalies (δV_p and δV_s) are then calculated using η , V_{p0} and V_{s0} in this layer, and the apparent thickness for this layer is calculated using eq. (2). The apparent depth is the sum of the apparent thickness of the individual layers.

While, in principle, the resulting apparent depths could easily be converted into true depths using eq. (2) and *P*- and *S*-wave velocity models obtained from previous seismic tomography studies, we choose not to do so for several reasons. The first is that there are some significant discrepancies among existing models, especially for the existence and magnitude of velocity anomalies in the MTZ, which directly affect the reliability of the resulting true thickness of the MTZ (Debaille *et al.* 2001; Grand 2002; Chang & van der Lee 2011; Hansen *et al.* 2012). Secondly, due to the previous paucity of broadband seismic data on the west side of the Red Sea, there is a lack of high-resolution seismic tomography models beneath Egypt. Thirdly, possible errors in tomographic models can lead to misleading results regarding MTZ thickness and the depths of the MTZ discontinuities. To illustrate the last point, we consider a simple scenario of a normal velocity structure above the *d*660 and flat *d*410 and *d*660 beneath an area (Fig. 3a), and using eq. (2) to calculate the resulting artificial undulations of the MTZ discontinuities when velocity anomalies are erroneously introduced. Under the conditions shown in Fig. 3(a), the apparent and true depths would be the same. However, if a tomographic inversion erroneously determined an LVZ in the MTZ and the resulting velocity model was used to correct the apparent depths, the corrected depth of the *d*660 as well as the corrected MTZ thickness would be reduced, resulting in the misleading conclusion that the lower MTZ is hotter-than-normal (Fig. 3b). Similarly, if one uses superficial upper-mantle velocities that are higher than the true velocities for depth corrections, an artificial depression of both the *d*410 and the *d*660 would be obtained (Fig. 3c). These combinations may lead to a depressed *d*410, an uplifted *d*660, a thinned MTZ and

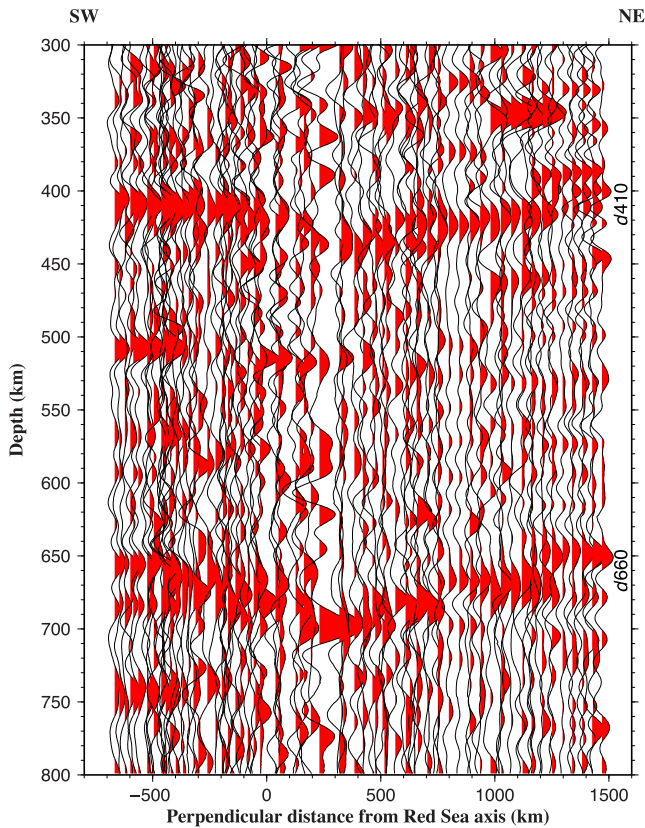


Figure 4. Results of stacking the moveout-corrected RFs, plotted by their perpendicular distance from the Red Sea axis.

an MTZ with lower-than-normal seismic velocities (Fig. 3d), which are ‘perfect proofs’ of a hot mantle plume originating from the lower mantle. Such unfortunate combinations are possible due to the limited vertical resolution of seismic (especially body wave) tomography, especially when the ray coverage is inadequate.

3 RESULTS

In order to obtain reliable measurements, we visually check each of the resulting depth series to select those with clear $d410$ or $d660$ arrivals, and we manually set a search window to find the depth corresponding to the maximum stacking amplitude for the $d410$ or the $d660$. On a small fraction of the time-series, multiple $d410$ or $d660$ arrivals are observed. In such cases, we choose the one with similar depths as neighbouring circles. Note that the robustness of the $d410$ and $d660$ arrivals observed on the vast majority of the resultant traces (Fig. 4) suggests that the spatial distribution of the discontinuity depths (and thus the main conclusions from the study) would remain the same when the traces with multiple arrivals are excluded.

Prominent peaks for the $d410$ and $d660$ are observed on the resulting depth series (Fig. 4). Beneath the study area, the mean depth of the $d410$ is 416 ± 13 km, that of the $d660$ is 674 ± 15 km, and the mean MTZ thickness is 257 ± 8 km. Note that the errors reflect the spatial variation of the measurements and not the standard deviations of the individual depth determinations (Cao & Levander 2010). Thus, the apparently large errors in the mean depths and thickness reflect significant changes between the observed values among the circles. Several remarkable characteristics in the apparent depths of the MTZ discontinuities can be observed (Figs 5 and 6).

First, the depths of both the $d410$ and $d660$, when plotted against the distance from the Red Sea axis, are approximately V-shaped (Figs 5 and 6). At the western end of the profile, the depths of the $d410$ and $d660$ are about 410 and 660 km, respectively. The discontinuities deepen towards the central part of the profile from both the west and east. Secondly, the area with the greatest MTZ discontinuity depths is not beneath the Red Sea axis, but is along the axis of the AAD (Figs 5–7). The maximum depression of about 30 km for the $d410$ and 45 km for the $d660$ is found near the axis of the AAD (Fig. 7). Thirdly, the depths of the $d410$ and those of the $d660$ are highly correlated, with a cross-correlation coefficient (XCC) of 0.81 and a slope of 1.14 ± 0.04 (Fig. 8). Fourthly, in spite of the significant asymmetry in surface elevation, volcanics and recent tectonic activity across the Red Sea, the MTZ thickness beneath the African and Arabian sides are statistically identical (i.e. 263 ± 14 km beneath Africa and 254 ± 8 km beneath Arabia; Fig. 6). Similarly, results on the western side of the AAD axis have a mean thickness of 261 ± 13 km, and those on the eastern side have a mean thickness of 254 ± 8 km (Fig. 7). Finally, the area beneath the central and western part of the AAD, approximately from -400 to 600 km from the Red Sea axis (Fig. 6), is characterized by the greatest MTZ thickness of 268 ± 10 km in the study area. The average thickness beneath the western part of the profile (from -700 to -400 km from the Red Sea axis) is 248 ± 5 km which is significantly thinner than the former area. Interestingly, the eastern end of the area with thick MTZ is approximately the eastern boundary of the zone with a thin lithosphere (Hansen *et al.* 2007).

In addition to $d410$ and $d660$, other possible discontinuities can be observed at the depths of 510 and 750 km, respectively (Fig. 4). The one at 510 km is a nearly horizontal feature that can be observed across the entire array, and the one at 750 km is mostly beneath the western end of the profile. Whether they represent real discontinuities or artefacts cannot be determined due to their weak amplitudes relative to the noise. If we assume that the apparent deepening of the $d410$ and $d660$ towards the AAD axis is mostly the result of upper-mantle velocity anomalies (see Section 4.2), the fact that the one at 510 km does not parallel to the $d410$ or $d660$ suggests that it may not be a true discontinuity.

4 DISCUSSION

4.1 Factors contributing to the observed depression of the MTZ discontinuities

Relative to the westernmost part of the study area, where the $d410$ and $d660$ depths are comparable with global averages, the maximum apparent depression of the $d410$ is about 30 km and that of the $d660$ is about 45 km beneath the AAD (Figs 6 and 7). In addition, compared to the MTZ thickness of 250 km in the IASP91 earth model, the regionally averaged apparent MTZ thickness ranges from being normal at the western end of the profile to about 10 km greater beneath the eastern part of the profile. At its maximum, the MTZ is about 15 km thicker beneath the central part of the profile (Fig. 6).

The observed apparent depths of the discontinuities may result from the following factors:

(1) Existence of velocity anomalies above the discontinuities. Using eq. (2) and by assuming a V_s and V_p relative anomaly ratio $[d\ln(V_s)/d\ln(V_p)]$ of 2.0, we estimate that a -1 per cent V_p anomaly in the upper mantle (0–410-km depth range) would result in an apparent depression of about 15 km for both MTZ discontinuities. Similarly, a V_p anomaly of -2 per cent would result in a 30-km

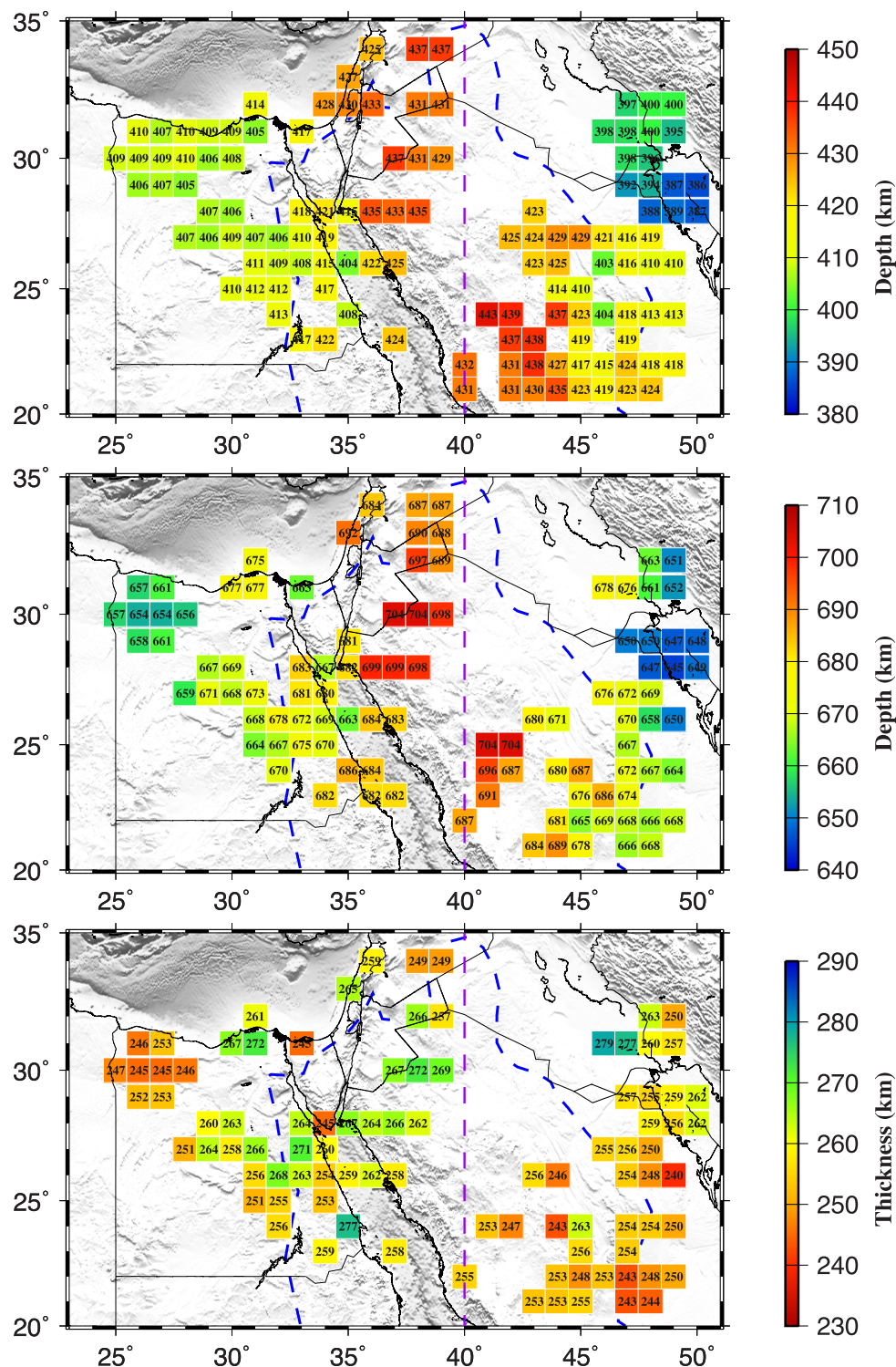


Figure 5. Resulting $d410$ depth (top panel), $d660$ depth (middle panel) and MTZ thickness (bottom panel). The purple dashed line is the AAD axis, and the blue dashed line outlines the ADD.

apparent depression. Note that the use of a $d\ln(V_s)/d\ln(V_p)$ of 2.0 is consistent with the P - and S -wave tomography results of Park *et al.* (2007) for Arabia.

(2) Temperature anomalies in the vicinity of the discontinuities. Using Clapeyron slopes of 2.9 and -2.1 MPa K^{-1} for the $d410$ and $d660$, respectively (Bina & Helffrich 1994), a 300 °C increase in temperature would lead to a 25-km depression of the $d410$ and a

17-km uplift of the $d660$. The effect of temperature is complicated when the temperature is anomalously high. Mineral physics experiments suggest that if the temperature at the bottom of the MTZ is higher than 1700 °C, the dominant phase transition would no longer be ringwoodite to perovskite, which has a negative Clapeyron slope. Instead, the transition from majorite to perovskite, which has a positive Clapeyron slope of about 1.0 MPa K^{-1} , would dominate

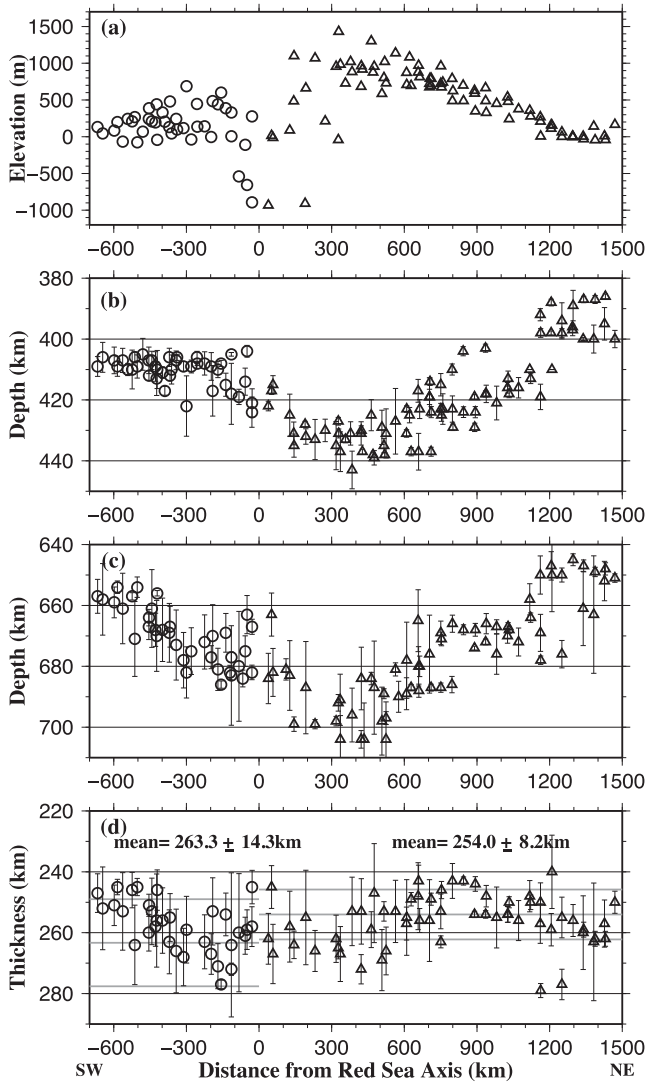


Figure 6. (a) Elevation, (b) depth of the d_{410} , (c) depth of the d_{660} and (d) MTZ thickness, plotted by their perpendicular distance from the Red Sea axis. The grey horizontal bars represent the mean and mean \pm one standard deviation of the observed MTZ thickness values for the African and Arabian plates. Circles are measurements on the African side, and triangles are those on the Arabian side.

(Hirose 2002). Furthermore, the effects of velocity anomalies and temperature anomalies, which are related through the scaling parameter $dV_p/dT = -4.8 \times 10^{-4} \text{ km s}^{-1} \text{ } ^\circ\text{C}^{-1}$ (Deal *et al.* 1999), are closely correlated. For instance, in the vicinity of the d_{410} , where V_p is about 9 km s^{-1} , a 1 per cent reduction of V_p corresponds to a temperature increase of about 190°C . This, in turn, corresponds to a 15-km depression of the d_{410} . Similarly, a -1 per cent velocity anomaly in the MTZ leads to an 8-km apparent depression of the d_{660} . However, if the anomaly reaches the d_{660} , the 190°C temperature anomaly would result in a 11-km uplift of the d_{660} , leading to a net apparent d_{660} uplift of 3 km.

(3) Presence of water in the MTZ. Previous studies have suggested that water has a similar effect as low temperature on the undulation of the MTZ discontinuities (Litasov *et al.* 2005). Water was involved to explain observed large (more than 30 km) depression of the d_{660} beneath the northern Colorado Plateau (Cao & Levander 2010).

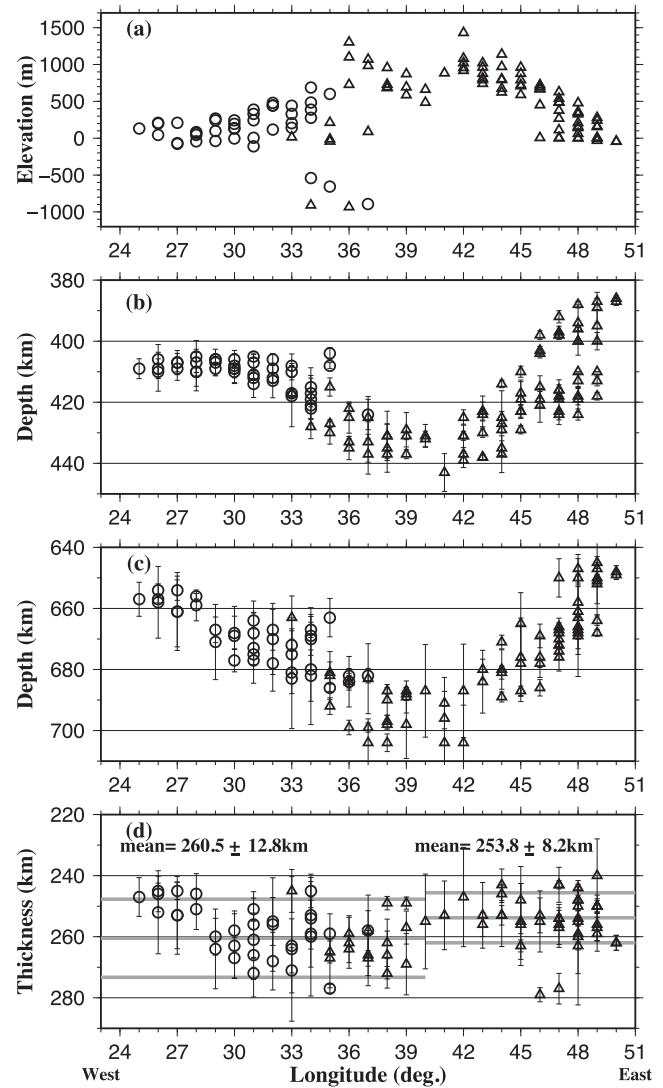


Figure 7. Same as Fig. 6 but plotted by longitude. The axis of the Afro-Arabian Dome is at about 40°E .

In the following discussions, we present several models (Fig. 9) with low-velocity anomalies that have different depth extents beneath the AAD, and explore their consistency with the observed spatial distribution of the MTZ discontinuity depths. We also explore the possibility of water in the MTZ and the expected effects of majorite-to-perovskite transition across the d_{660} . Note that although Clapeyron slopes given by Bina & Helffrich (1994) are used below, the use of different values provided by other studies (e.g. Ito & Takahashi 1989; Fei *et al.* 2004) would not significantly change the main conclusions. The same is true if a different dV_p/dT scaling factor or a different $d\ln(V_s)/d\ln(V_p)$ value is used.

4.2 Possible models to explain the observations

4.2.1 Model A

In this model (Fig. 9), the LVZ is limited to the upper mantle (0–410 km). The high positive correlation between the observed apparent depths of the d_{410} and the d_{660} (Fig. 8) suggests that most of the apparent depression of the discontinuities is the result of lower-than-normal velocity anomalies above the d_{410} . If

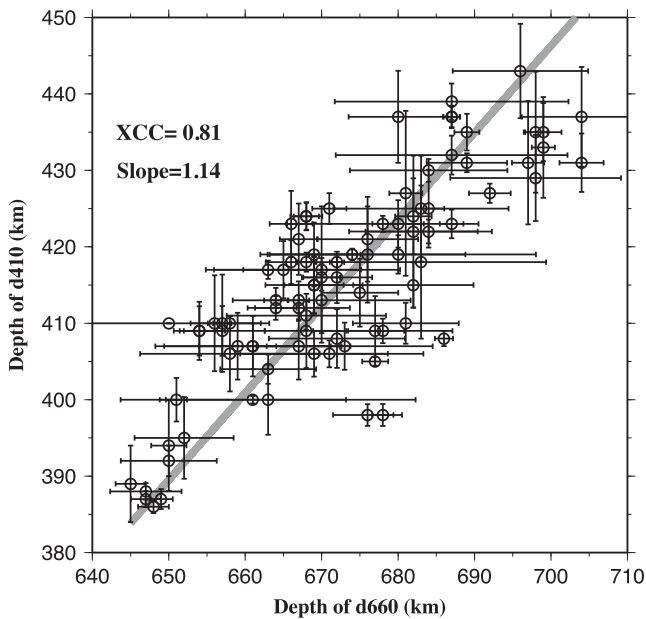


Figure 8. Correlation between the observed depths of the d_{410} and d_{660} . The error bars represent one standard deviation, and the thick grey line is the result of least-squares fitting.

we assume a mean upper-mantle V_p anomaly of -2.0 per cent, which is similar to the results of most seismic tomography studies (Benoit *et al.* 2003; Park *et al.* 2007; Chang & van der Lee 2011), a 30-km apparent depression of both d_{410} and d_{660} should be observed. This is comparable with the observed amount of depression of the d_{410} , but is smaller than that observed for the d_{660} .

4.2.2 Model B

For this model, the LVZ extends to the uppermost MTZ and reaches the d_{410} . Using the scaling parameter between V_p and temperature, a -2.0 per cent V_p anomaly corresponds to a temperature increase of about 375°C , which results in an additional ~ 30 -km depression of the d_{410} . Thus, the total depression of the d_{410} would be 60 km, which is twice of the observed value (Model B1 in Fig. 9). To match the observed depression of the d_{410} , the V_p anomaly in the upper mantle and surrounding the d_{410} needs to be reduced to -1 per cent. This anomaly, however, results in an ~ 15 -km apparent depression of the d_{660} , which is only about 1/3 of the observed value. Note that this model is referred to as Model B2 in Fig. 9.

4.2.3 Model C

This model includes an LVZ with an amplitude of -1 per cent, extending from the surface to the lowermost MTZ, but it does not reach the d_{660} . In this case, the apparent depression of the d_{410} is still 30 km, but that of the d_{660} is 23 km, which is about 1/2 of the observed value. Note that the -1 per cent V_p anomaly in the MTZ leads to an additional 8 km apparent depression of the d_{660} relative to the situation when the anomaly is restricted to the upper mantle (Model B2 in Fig. 9).

4.2.4 Model D

This model is the same as Model C, but the LVZ extends to beneath the MTZ (to an arbitrary depth because velocity anomalies

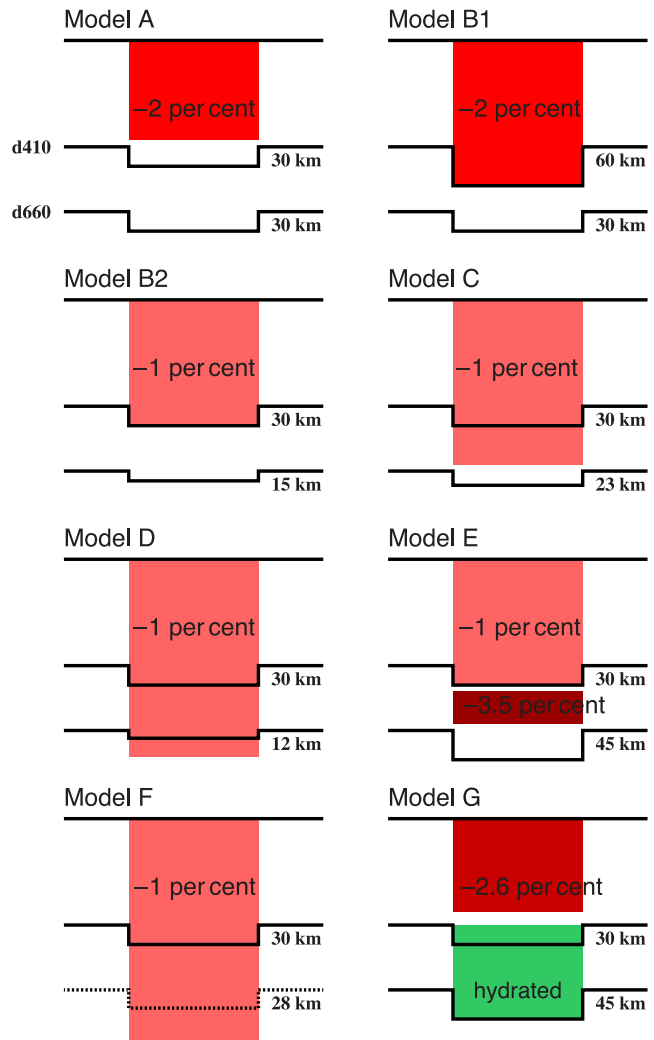


Figure 9. Schematic models to explain the observed depressions of the MTZ discontinuities. See Section 4.2 for descriptions about each of the models. In Model F, the dashed d_{660} represents majorite to perovskite phase transition. Note that there is a $2.5\times$ vertical exaggeration for the amplitude of the depressions.

beneath the d_{660} have no effects on the depths of the MTZ discontinuities). This model is analogous to a mantle plume originated from the lower mantle. Relative to Model C, the amount of apparent depression of the d_{660} reduces due to uplift of the d_{660} associated with the high temperature. As discussed in Section 4.1, a -1.0 per cent V_p anomaly corresponds to a temperature increase of about 190°C , which leads to a 11-km uplift of the d_{660} . The total depression of the d_{660} under this model is thus 12 km, as a result of a 11-km uplift from the 23-km depression in Model C (Fig. 9).

4.2.5 Model E

Given the contrasting effects of velocity and temperature anomalies on the depth of the d_{660} , a strong LVZ in the MTZ but which does not extend to the d_{660} is needed to match our observations. For the observed 45-km depression of the d_{660} , a V_p anomaly as large as about -3.5 per cent is needed in the MTZ (and -1 per cent in the upper mantle). This anomaly in the MTZ is not observed by any of the previous seismic tomography studies. The only possible exception is the model presented by Chang & van

der Lee (2011) who proposed an ~ 5 per cent shear wave velocity anomaly in the uppermost MTZ and a much smaller anomaly in the middle and lower MTZ. However, because in the velocity model the LVZ reaches the $d410$ and the rest of the MTZ has normal or slightly negative velocity anomalies, the $d410$ is expected to be deeper than the $d660$ (Model B1). This is inconsistent with the observations (Fig. 6). Another problem with Model E is that there is no physical mechanism to restrain the LVZ in the MTZ so that it does not reach the $d410$ or the $d660$.

4.2.6 Model F

This model assumes a majorite-to-pervoskite transition across the $d660$. If we assume a V_p anomaly of -1 per cent extending from the surface to beneath the $d660$, the apparent depression of the $d660$ due to the velocity anomaly is 23 km (Model C), and the corresponding temperature increase is about 190 °C. Given the approximate $+1.0 \text{ MPa K}^{-1}$ Clapeyron slope associated with this phase transition, the corresponding depression of the $d660$ caused by this increased temperature is only about 5 km, leading to a total depression of less than 30 km. A temperature anomaly of about 570 °C is needed in the region surrounding the $d660$ to match the 45-km apparent depression, but such a temperature anomaly requires a -3 per cent V_p anomaly, which is not found in any of the existing seismic tomographic models.

4.2.7 Model G

This model advocates for the effects of a hydrated MTZ on the observed MTZ discontinuity depths. An increasing number of mineral physics experiments suggest that water in the MTZ can lead to uplift of the $d410$ and depression of the $d660$ (e.g. Kohlstedt *et al.* 1996; Smyth & Frost 2002; Litasov *et al.* 2005; Smyth *et al.* 2006; Cao & Levander 2010), and thus can account for the observed 15-km thickening of the MTZ relative to the global average. If we assume that water causes an 8-km uplift of the $d410$ and the same amount of depression of the $d660$, a mean V_p anomaly of -2.6 per cent in the upper mantle, which results in a 38-km apparent depression of both discontinuities, can explain the observed 30 and 45-km depression of the $d410$ and $d660$, respectively (see Model G in Fig. 9 and Section 4.3 for additional information).

4.3 Implications on the formation and evolution of the Red Sea and the AAD

As discussed above, the model that can most satisfactorily explain the observed spatial distribution of the $d410$ and $d660$ beneath the AAD involves an upper-mantle LVZ with a V_p anomaly of about -2.6 per cent and a hydrated MTZ (Kohlstedt *et al.* 1996). We speculate that one of the likely mechanisms to bring water to the MTZ is through the subduction of oceanic slabs (Nolet & Zielhuis 1994). Located adjacent to the northeast edge of the Africa-Arabian Plate, the MTZ beneath the AAD is a plausible locale for the accommodation of oceanic slabs subducted in the pre-Cambrian. Interestingly, surface geological investigations have suggested that prior to the onset of the rapid uplift of the AAD at 14 Ma, uplift of the western part of Arabia relative to the eastern part started at about 750 Ma, and the uplift was accompanied by igneous activity (Stern & Johnson 2010). This long-lasting uplift and igneous activity could be associated with a hydration-induced LVZ and partial-melting

of the upper mantle resulting from upward migration of water in the MTZ.

Previous studies suggested that 2.0 wt per cent of water incorporated in the MTZ can lead to a 10–30-km elevation of the $d410$ and a 15-km depression of the $d660$ (see Cao & Levander 2010 for details), resulting in a 25–45-km thickening of the MTZ. Thus the observed 15-km thickening beneath the AAD suggests that at the present time, the amount of water in the MTZ is significantly less than 2.0 wt per cent, probably due to gradual release of water to the upper mantle since 750 Ma. Under the assumption that the amount of water and that of MTZ thickening are linearly correlated, the estimated amount of water at the present time beneath the AAD is approximately 1 wt per cent. We emphasize that this model (Model G), while it is the most reasonable among all the possible models (Fig. 9) in explaining the observed spatial variations of the MTZ discontinuity depths, is preliminary and it alone cannot satisfactorily explain temporal variations in the chemical composition of continental magmatism observed in western Arabia (Camp & Roobol 1992). Another problem with this model is that it does not allow significant relative movement between the MTZ and the surface of the Earth in the study area. Alternatively, the water could be brought into the MTZ recently and has no role in the volcanism on the AAD. Clearly, addition work is needed to identify the source of the proposed hydration of the MTZ. Our measurements, however, are inconsistent with the proposed existence of one or more active mantle plumes beneath the study area (Dixon *et al.* 1989; Camp & Roobol 1992; Chang & van der Lee 2011). It must be mentioned that given the spatial coverage of the RFs used in this study (Fig. 1), the possibility that there exists one or more small-scale plumes cannot be completely ruled out. In addition, a lack of plumes at the present time does not preclude the existence of plumes in the past.

Another significant characteristic of our observations is that the Red Sea is not associated with significant apparent thickening of the upper mantle. Such a thickening would be expected if the upper mantle beneath the Red Sea has slower seismic velocities. This is consistent with most seismic tomography results, where the Red Sea is not found to be underlain by particularly low velocities in the upper mantle compared to those observed beneath the AAD (Park *et al.* 2007; Park *et al.* 2008; Sicilia *et al.* 2008; Chang & van der Lee 2011; Hansen *et al.* 2012). On the other hand, our measurements rule out the possibility that the Red Sea is underlain by a zone of mantle upwelling originated from beneath the MTZ. Such a lower-mantle upwelling would produce a thinner-than-normal MTZ beneath the Red Sea, which is not observed.

5 CONCLUSIONS

For the first time, systematic apparent deepening of both the $d410$ and $d660$ towards the axis of the AAD from both the African and the Arabian sides is revealed using broad-band seismic data recorded on both sides of the northern Red Sea. The magnitude of the apparent depression of the $d410$ is about 30 km, and that of the $d660$ is about 45 km. The observations can be satisfactorily explained by the combined effects of an LVZ in the upper mantle, which artificially depresses both discontinuities by about 38 km, and water in the MTZ, which actually uplifts the $d410$ and depresses the $d660$ by about 8 km. The present existence of one or more mantle plumes originating in the MTZ or in the lower mantle beneath the northern part of the AAD or the northern Red Sea is not supported by the observed depth variations of the MTZ discontinuities.

ACKNOWLEDGEMENTS

Data used in this study were obtained from the ENSN and IRIS DMC. Critical reviews by S. E. Hansen and an anonymous reviewer significantly improved the manuscript. AAM acknowledges the Egyptian Science and Technology Development Fund for support during the course of the study. This study was partially supported by the US National Science Foundation under grants EAR-1009946 and 1030230.

REFERENCES

- Al-Damegh, K., Sandvol, E. & Barazangi, M., 2005. Crustal structure of the Arabian Plate: new constraints from the analysis of teleseismic receiver functions, *Earth planet. Sci. Lett.*, **231**, 177–196.
- Almond, D.C., 1986. Geological evolution of the Afro-Arabian Dome, *Tectonophysics*, **131**, 301–332.
- Altherr, R., Henjes-Kunst, F. & Baumann, A., 1990. Asthenosphere versus lithosphere as possible sources for basaltic magmas erupted during formation of the Red Sea: constraints from Sr, Pb and Nd isotopes, *Earth planet. Sci. Lett.*, **96**, 269–286.
- Ammon, C.J., 1991. The isolation of receiver effects from teleseismic *P*-waveforms, *Bull. seism. Soc. Am.*, **81**, 2504–2510.
- Andrews, J. & Deuss, A., 2008. Detailed nature of the 660 km region of the mantle from global receiver function data, *J. geophys. Res.*, **113**, B06304, doi:10.1029/2007JB005111.
- Benoit, M.H., Nyblade, A.A., VanDecar, J.C. & Gurrrola, H., 2003. Upper mantle *P* wave velocity structure and transition zone thickness beneath the Arabian Shield, *Geophys. Res. Lett.*, **30**, 1531, doi:10.1029/2002GL016436.
- Bina, C.R. & Helffrich, G., 1994. Phase transition Clapeyron slopes and transition zone seismic discontinuity topography, *J. geophys. Res.*, **99**, 15 853–15 860.
- Bosworth, W., Huchon, P. & McClay, K., 2005. The Red Sea and Gulf of Aden basins, *J. Afr. Earth Sci.*, **43**, 334–378.
- Camp, V.E. & Roobol, M.J., 1992. Upwelling asthenosphere beneath western Arabia and its regional implications, *J. geophys. Res.*, **97**, 15 255–15 271.
- Cao, A. & Levander, A., 2010. High-resolution transition zone structures of the Gorda slab beneath the western United States: implication for deep water subduction, *J. geophys. Res.*, **115**, B07301, doi:10.1029/2009JB006876.
- Chang, S. *et al.*, 2010. Joint inversion for three dimensional *S* velocity mantle structure along the Tethyan margin, *J. geophys. Res.*, **115**, B08309, doi:10.1029/2009JB007204.
- Chang, S.J. & van der Lee, S., 2011. Mantle plumes and associated flow beneath Arabia and East Africa, *Earth planet. Sci. Lett.*, **302**, 448–454.
- Chang, S.J., Merino, M., van der Lee, S., Stein, S. & Stein, C.A., 2011. Mantle flow beneath Arabia offset from the opening Red Sea, *Geophys. Res. Lett.*, **38**, L04301, doi:10.1029/2010GL045852.
- Civetta, L., La Volpe, L. & Lirer, L., 1978. K-Ar ages of the Yemen Plateau, *J. Volc. Geotherm. Res.*, **4**, 307–314.
- Daradich, A., Mitrovica, J.X., Pysklywec, R.N., Willett, S.D. & Forte, A.M., 2003. Mantle flow, dynamic topography, and rift-flank uplift of Arabia, *Geology*, **31**, 901–904.
- Deal, M.M., Nolet, G. & van der Hilst, R.D., 1999. Slab temperature and thickness from seismic tomography: 1. Method and application to Tonga, *J. geophys. Res.*, **38**, 28 789–28 802.
- Debayle, E., Leveque, J.-J. & Cara, M., 2001. Seismic evidence for a deeply rooted low-velocity anomaly in the upper mantle beneath the northeastern Afro/Arabian continent, *Earth planet. Sci. Lett.*, **193**, 423–436.
- Dixon, T.H., Ivins, E.R. & Franklin, B.J., 1989. Topographic and volcanic asymmetry around the Red Sea: constraints on rift models, *Tectonics*, **8**, 1193–1216.
- Efron, B. & Tibshirani, R., 1986. Bootstrap methods for standard errors, confidence intervals, and other measures of statistical accuracy, *Stat. Sci.*, **1**, 54–75.
- Elsheikh, A.A., Gao, S.S., Liu, K.H., Mohamed, A.A., Yu, Y. & Fat-Helbary, R.E., 2014. Seismic anisotropy and subduction-induced mantle fabrics beneath the Arabian and Nubian plates adjacent to the Red Sea, *Geophys. Res. Lett.*, **41**, 2376–2381.
- Fei, Y., Van Orman, J., Li, J., Van Westrenen, W., Sanloup, C., Minarik, W. & Funakoshi, K.I., 2004. Experimentally determined postspinel transformation boundary in Mg_2SiO_4 using MgO as an internal pressure standard and its geophysical implications, *J. geophys. Res.*, **109**, B02305, doi:10.1029/2003JB002562.
- Gao, S.S. & Liu, K.H., 2014. Mantle transition zone discontinuities beneath the contiguous United States, *J. geophys. Res.*, **119**, doi:10.1002/2014JB011253.
- Gao, S.S., Silver, P.G. & Liu, K.H., 2002. Mantle discontinuities beneath southern Africa, *Geophys. Res. Lett.*, **29**, 1291–1294.
- Grand, S.P., 2002. Mantle shear wave tomography and the fate of subducted slabs, *Phil. Trans. R. Soc. Lond. A*, **360**, 2475–2491.
- Hansen, S., Schwartz, S., Al-Amri, A. & Rodgers, A., 2006. Combined plate motion and density-driven flow in the asthenosphere beneath Saudi Arabia: evidence from shear-wave splitting and seismic anisotropy, *Geology*, **34**, 869–872.
- Hansen, S., Rodgers, A., Schwartz, S. & Al-Amri, A., 2007. Imaging ruptured lithosphere beneath the Red Sea and Arabian Peninsula, *Earth planet. Sci. Lett.*, **259**, 256–265.
- Hansen, S.E., Nyblade, A.A. & Benoit, M.H., 2012. Mantle structure beneath Africa and Arabia from adaptively parameterized *P*-wave tomography: implications for the origin of Cenozoic Afro-Arabian tectonism, *Earth planet. Sci. Lett.*, **319**, 23–34.
- Hirose, K., 2002. Phase transitions in pyrolitic mantle around 670-km depth: implications for upwelling of plumes from the lower mantle, *J. geophys. Res.*, **107**, 2078, doi:10.1029/2001JB000597.
- Ito, E. & Takahashi, E., 1989. Postspinel transformations in the system $\text{Mg}_2\text{SiO}_4\text{--Fe}_2\text{SiO}_4$ and some geophysical implications, *J. geophys. Res.*, **94**, 10 637–10 646.
- Jasbinsek, J.J., Duker, K.G. & Hansen, S.M., 2010. Characterizing the 410 km discontinuity low-velocity layer beneath the LA RISTRA array in the North American Southwest, *Geochem. Geophys. Geosyst.*, **11**, Q03008, doi:10.1029/2009GC002836.
- Kohlstedt, D.L., Keppler, H. & Rubie, D.C., 1996. Solubility of water in the α , β and γ phases of $(\text{Mg,Fe})_2\text{SiO}_4$, *Contrib. Mineral. Petrol.*, **123**, 345–357.
- Kumar, M.R., Ramesh, D.S., Saul, J., Sarkar, D. & Kind, R., 2002. Crustal structure and upper mantle stratigraphy of the Arabian shield, *Geophys. Res. Lett.*, **29**, 1301–1304.
- Lazar, M., Ben-Avraham, Z. & Garfunkel, Z., 2012. The Red Sea—new insights from recent geophysical studies and the connection to the Dead Sea fault, *J. Afr. Earth Sci.*, **68**, 96–110.
- Litasov, K.D., Ohtani, E., Suzuki, A. & Funakoshi, K., 2005. Wet subduction versus cold subduction, *Geophys. Res. Lett.*, **32**, L13312, doi:10.1029/2005GL022921.
- Liu, K.H. & Gao, S.S., 2006. Mantle transition zone discontinuities beneath the Baikal rift and adjacent areas, *J. geophys. Res.*, **111**, B11301, doi:10.1029/2005JB004099.
- Liu, K.H. & Gao, S.S., 2010. Spatial variations of crustal characteristics beneath the Hoggar swell, Algeria revealed by systematic analyses of receiver functions from a single seismic station, *Geochem. Geophys. Geosyst.*, **11**, Q08011, doi:10.1029/2010GC003091.
- Liu, K.H., Gao, S.S., Silver, P.G. & Zhang, Y., 2003. Mantle layering across central South America, *J. geophys. Res.*, **108**, 2510, doi:10.1029/2002JB002208.
- McGuire, A.V. & Bohannon, R.G., 1989. Timing of mantle upwelling: evidence for a passive origin for the Red Sea Rift, *J. geophys. Res.*, **94**, 1677–1682.
- Mechie, J. & Prodehl, C., 1988. Crustal and uppermost mantle structure beneath the Afro-Arabian rift system, *Tectonophysics*, **153**, 103–121.
- Nolet, G. & Zielhuis, A., 1994. Low *S* velocities under the Tornquist-Teisseyre zone: evidence for water injection into the transition zone by subduction, *J. geophys. Res.*, **99**, 15 813–15 821.

- Nyblade, A.A., Knox, R.P. & Gurrola, H., 2000. Mantle transition zone thickness beneath Afar: implications for the origin of the Afar hotspot, *Geophys. J. Int.*, **142**, 615–619.
- Ohtani, E. & Litasov, K.D., 2006. The effect of water on mantle phase transitions, *Rev. Mineral. Geochem.*, **62**, 397–420.
- Pallister, J.S., McCausland, W.A., Jonsson, S., Lu, Z., Zahran, H.M., El Hadidy, S. & Moufti, M.R., 2010. Broad accommodation of rift-related extension recorded by dyke intrusion in Saudi Arabia, *Nature Geosci.*, **3**, 705–712.
- Park, Y., Nyblade, A.A., Rodgers, A.J. & Al-Amri, A., 2007. Upper mantle structure beneath the Arabian Peninsula and northern Red Sea from teleseismic body wave tomography: implications for the origin of Cenozoic uplift and volcanism in the Arabian Shield, *Geochem. Geophys. Geosyst.*, **8**, Q06021, doi:10.1029/2006GC001566.
- Park, Y., Nyblade, A.A., Rodgers, A.J. & Al-Amri, A., 2008. S wave velocity structure of the Arabian Shield upper mantle from Rayleigh wave tomography, *Geochem. Geophys. Geosyst.*, **9**, Q07020, doi:10.1029/2007GC001895.
- Ringwood, A.E., 1975. *Composition and Petrology of the Earth's Mantle*, McGraw-Hill.
- Ritsema, J., van Heijst, H.J. & Woodhouse, J.H., 1999. Complex shear wave velocity structure imaged beneath Africa and Iceland, *Science*, **286**, 1925–1928.
- Rodgers, A., Walter, W., Mellors, R., Al-Amri, A. & Zhang, Y., 1999. Lithospheric structure of the Arabian Shield and Platform from complete regional waveform modeling and surface wave group velocities, *Geophys. J. Int.*, **138**, 871–878.
- Sandvol, E., Seber, D., Barazangi, M., Vernon, F., Mellors, R. & Al-Amri, A., 1998. Lithospheric seismic velocity discontinuities beneath the Arabian Shield, *Geophys. Res. Lett.*, **25**, 2873–2876.
- Seber, D. & Mitchell, B., 1992. Attenuation of surface waves across the Arabian peninsula, *Tectonophysics*, **204**, 137–150.
- Shearer, P.M., 1991. Constraints on upper mantle discontinuities from observations of long-period reflected and converted phases, *J. geophys. Res.*, **96**, 18 147–18 182.
- Sicilia, D. *et al.*, 2008. Upper mantle structure of shear-waves velocities and stratification of anisotropy in the Afar Hotspot region, *Tectonophysics*, **462**, 164–177.
- Smyth, J.R. & Frost, D.J., 2002. The effect of water on the 410-km discontinuity: an experimental study, *Geophys. Res. Lett.*, **29**, 1231–1234.
- Smyth, J.R., Frost, D.J., Nestola, F., Holl, C.M. & Bromiley, G., 2006. Olivine hydration in the deep upper mantle: effects of temperature and silica activity, *Geophys. Res. Lett.*, **33**, L15301, doi:10.1029/2006GL026194.
- Stern, R.J. & Johnson, P., 2010. Continental lithosphere of the Arabian Plate: a geologic, petrologic, and geophysical synthesis, *Earth Sci. Rev.*, **101**, 29–67.
- Wolfe, C.J., Vernon, F.L. & Al-Amri, A., 1999. Shear-wave splitting across western Saudi Arabia: the pattern of upper mantle, anisotropy at a Proterozoic Shield, *Geophys. Res. Lett.*, **26**, 779–782.